Targeting mitochondrial protease in diffuse gliomas

Olga Kim[1,#], Jinkyu Jung[1,#], Shaunak Sathe[1], Guangyang Yu[1], Zach Sergi[1], Qi Li[1], Peng Lu[1], Meili Zhang[1], Ru-Ching Hsia[2], Michael J. Kruhlak[3], Raj Chari[4], Herui Wang[1], Bao Tran[5], Ronald J. Holewinski[6], Marina Chan[7], Thorkell Andresson[6], Zheng-Gang Liu[8], Lee M. Graves[9], Taranjit S. Gujral[7], Edwin J. Iwanowicz[10], Jing Wu[1,*]

[1] Neuro-Oncology Branch, Center for Cancer Research, National Cancer Institute, National Institutes of Health, Bethesda, MD 20892, USA
[2] Electron Microscopy Laboratory, Leidos Biomedical Inc / Frederick National Laboratory for Cancer Research, Frederick, MD 21701, USA
[3] CCR Confocal Microscopy Core Facility, Laboratory of Cancer Biology and Genetics, Center for Cancer Research, National Cancer Institute, National Institutes of Health, Bethesda, MD 20892, USA
[4] Genome Modification Core laboratory, Leidos Biomedical Inc / Frederick National Laboratory for Cancer Research, Frederick, MD 21701, USA
[5] Sequencing Facility, Leidos Biomedical Inc / Frederick National Laboratory for Cancer Research, Frederick, MD 21701, USA
[6] Protein Characterization Laboratory, Leidos Biomedical Inc / Frederick National Laboratory for Cancer Research, Frederick, MD 21701, USA
[7] Human Biology Division, Fred Hutchinson Cancer Center, Seatttle, WA 98109, USA
[8] Laboratory of Immune Cell Biology, Center for Cancer Research, National Cancer Institute, National Institutes of Health, Bethesda, MD 20892, USA
[9] Department of Pharmacology and the Lineberger Comprehensive Cancer Center, University of North Carolina at Chapel Hill, Chapel Hill, NC 27599, USA
[10] Madera Therapeutics LLC, Chapel Hill, NC 27517, USA
[#] equally contributed

* Corresponding Author: Jing Wu, MD, PhD, Neuro-Oncology Branch, Center for Cancer Research, NCI, NIH, Building 37, Room 1142A, 37 Convent Drive, Bethesda, MD 20892, USA. Phone: 240-760-6036; e-mail: jing.wu3@nih.gov

Running title: Targeting ClpP against diffuse gliomas

Word count: 7,156

ABSTRACT

Caseinolytic protease proteolytic subunit (ClpP) is part of the mitochondrial ClpXP protease responsible for degrading damaged proteins in the matrix, thus maintaining metabolic homeostasis. Small molecule activators of ClpP (ClpP agonists) have recently shown great promise against metabolically active cancers. TR107, a novel ClpP activator, demonstrates potent and selective cytotoxicity against glioma cells at nanomolar concentrations. Compared to the FDA-approved ClpP agonist ONC201 (Dordaviprone), TR107 shows greater efficacy across patient-derived and isogenic glioma models. TR107 effects are ClpP-dependent and result in widespread mitochondrial dysfunction evident by extensive protein degradation, impaired OxPhos, reduced mtDNA copy number, and ATP depletion. These disruptions are more severe in IDH-mutant than IDH-wildtype glioma cells, leading to enhanced cell cycle arrest, apoptosis, and inhibition of mTOR/AKT/4EBP1 signaling pathway. In this study, we show that ClpP agonism demonstrates preferential anti-tumor activity against IDH-mutant glioma in *in vitro*, *ex vivo*, and *in vivo* models. These findings support TR107 as a promising new targeted therapeutic for IDH-mutant gliomas.

Keywords: diffuse glioma, IDH mutation, caseinolytic protease proteolytic subunit (ClpP), TR107, mitochondria.

INTRODUCTION

Mitochondria are essential multifaceted organelles required for cellular energy metabolism and survival, macromolecule biogenesis and lipid synthesis, maintenance of redox balance and regulation of apoptosis (1,2). Since, maintaining mitochondrial integrity plays an important role in ensuring cell viability and performance, targeting mitochondrial function has emerged as a promising therapeutic strategy in cancer treatment.

Caseinolytic protease proteolytic subunit (ClpP) is an ATP-dependent protease located in the mitochondrial matrix that participates in mitochondrial proteins quality control by degrading misfolded or damaged proteins (3). ClpP substrate pool includes proteins essential for TCA cycle, oxidative phosphorylation (OxPhos), mitochondrial gene transcription and translation, fatty acid and amino acid metabolism (4). It has been shown that hyperactivating ClpP leads to uncontrolled degradation of ClpP substrates resulting in the decreased levels of respiratory chain proteins, impaired OxPhos and cell death (3,5). These findings led to investigating the use of ClpP-targeting compounds as a novel therapeutic approach against cancer. ONC201 is the first-in-class imipridones that binds and activates human ClpP and is currently in clinical trials for multiple cancers, including H3K27M gliomas and glioblastomas (6,7). Based on its demonstrated clinical activity and mechanistic rationale, ONC201 has received FDA approval for the treatment of histone H3 K27M–mutant diffuse midline glioma (8). The clinical development of ONC201 was supported by preclinical studies showing that ClpP activation induces selective tumor cell lethality through mitochondrial proteostasis disruption and metabolic stress pathways. ONC201 depletes ATP, triggers mitochondrial structural and functional impairment, and inhibits multiple pathways disrupting cancer stem cell function in breast cancer cells (9,10). In contrast to ONC201, which was initially developed as a dopamine D2 receptor (DRD2) antagonist and activator of the TNF-related apoptosis-inducing ligand (TRAIL), TR107 was specifically designed to selectively target ClpP without off-target effects (e.g., DRD2 antagonism) demonstrating an excellent potency and affinity for ClpP in breast cancer and other tumor models (7). Administration of TR107 at the low nanomolar concentrations disruptes mitochondrial respiration and metabolism, resulting in tumor growth inhibition in both *in vitro* and *in vivo* models (11).

Isocitrate dehydrogenase (IDH)–mutant gliomas represent a distinct molecular subtype of diffuse glioma characterized by recurrent mutations in *IDH1* or *IDH2*, which confer neomorphic

enzymatic activity that converts α-ketoglutarate into the oncometabolite D-2-hydroxyglutarate (2-HG) (12). Accumulation of 2-HG leads to widespread epigenetic remodeling through inhibition of α-ketoglutarate–dependent dioxygenases, resulting in a hypermethylation phenotype and impaired cellular differentiation (13). In addition to epigenetic dysregulation, IDH-mutant glioma cells exhibit extensive metabolic reprogramming, including altered mitochondrial function, dependency on oxidative phosphorylation for survival, and increased sensitivity to disruptions in mitochondrial proteostasis (14). Emerging evidence suggests that these tumors are particularly dependent on mitochondrial quality control pathways, including the ClpP protease complex, to maintain bioenergetic homeostasis and survival under metabolic stress (7,15). These unique vulnerabilities may provide a strong rationale for therapeutically targeting mitochondrial pathways in IDH-mutant glioma. In this study, we aimed to investigate TR107 effects on adult diffuse gliomas and explore potential metabolic vulnerabilities that favor the use of TR107 in tumors with *IDH* mutations.

MATERIAL and METHODS

Cell culture, mycoplasma testing and chemicals

GSC923 cell line was cultured from the patient's glioblastoma tissue and generated by the Neuro-Oncology Branch laboratory at National Cancer Institute (NCI, obtained in 2016). GSC20 and GSC23 (RRID:CVCL_DR59), patient-derived GBM cells, were obtained from MD Anderson Cancer Center (Houston, TX, obtained in 2014). TS603, a patient-derived IDHmut astrocytoma, grade 3 cell line, was received from Dr. Timothy Chan, Memorial Sloan Kettering Cancer Center (New York, NY, obtained in 2018). BT142 (RRID:CVCL_D718), a patient-derived IDHmut oligoastrocytoma, grade 3 cell line, was purchased from ATCC (ACS-1018, obtained in 2021). BT142 mut/- is a glioma brain tumor stem cell line derived from the left frontal lobe of a 38-year-old, White male. BT142 mut/- contains a homozygous IDH1 R132H mutation, which originated from a heterozygous IDH1 R132H BT142 cells. MGG152, a patient-derived IDHmut astrocytoma, grade 4 cell line, was obtained from Dr. Daniel Cahill, The General Hospital Corp. d/b/a/ Massachusetts General Hospital (Boston, MA, obtained in 2019). GBM1-IDHwt and GBM1-IDHmut, patient-derived GBM cell lines, were kindly provided by Dr. Shuli Xia, Johns Hopkins University School of Medicine (Baltimore, MD, obtained in 2021). Glioma stem-like cells (GSCs) were grown in 3D spheroids in suspension. GSC923, GSC20, GSC23 (RRID:CVCL_DR59), MGG152, GBM1-IDHwt, and GBM1-IDHmut were cultured in NBE medium, composed of Neurobasal-A medium (Thermo Fisher Scientific, Waltham, MA), N2 and B27 supplements (Invitrogen, Carlsbad, CA) and recombinant human basic fibroblast growth factor (bFGF), epidermal growth factor (EGF), 1% penicillin/streptomycin (p/s), and 1 mmol/L of L-Glutamine (Thermo Fisher Scientific). TS603 and BT142 cells were cultured in DMEM/F12 medium (Thermo Fisher Scientific) supplemented with N2, 20 ng/mL of bFGF and EGF, 1% p/s, and 2 μg/mL of heparin sulfate (Sigma-Aldrich, St. Louis, MO). HA (human astrocytes) were cultured in DMEM/F12 medium, containing 10% fetal bovine serum (FBS), 8 mg/mL of D-glucose, 1% p/s, and 50 ng/mL of amphotericin. Accutase (Sigma-Aldrich) was used to dissociate neurospheres into single cells.

All cells were cultured at 37°C in a humidified incubator with 5% CO_2 and were routinely tested for Mycoplasma contamination using the MycoAlert™ Mycoplasma Detection Kit (Lonza, #LT07-318). Cell line authentication was performed by the originating institutions using short

tandem repeat (STR) profiling prior to receipt; no additional authentication was performed by our laboratory. All experiments were conducted using cells within 10 passages after thawing from frozen stocks generated upon receipt from the original source.

TR107 was provided by Madera Therapeutics LLC (patent number WO 2020/176654 A1, example 65, Chapel Hill, NC) (16). ONC201 (S7963) was purchased from Selleck Chemicals LLC (Houston, TX).

Cell viability assay

For cell viability analysis using Celigo Image Cytometer, the cells were seeded in 2D culture at 5-8x10^3 cells/well in 96-well plates in triplicates. Cell viability was determined using double staining of total cells with Hoechst 33342 and dead cells with Propidium Iodide (PI) and measured by Celigo Image cytometer, per manufacturer's protocol. The percent of viable cells was determined by the number of viable treated cells divided by the mean number of viable control cells.

Generation of ClpP KO cells

For *ClpP* KO, guide RNAs were designed using sgRNA Scorer 2.0 (17) and oligonucleotides corresponding to target sites GCGCCTATGACATCTACTCGCGG (CLPP KO#1) and GGAGCGCATCGTGTGCGTCATGG (CLPP KO#2) were cloned into the Lenti-CRISPR-V2 plasmid (RRID: Addgene_166482), as previously described (8). LentiCRISPR v2 was a gift from Feng Zhang (RRID: Addgene_52961).

Lentivirus was generated by co-transfection with psPAX2 (RRID: Addgene_12260) and pMD2.G (RRID: Addgene_12259) plasmids in HEK293T cells using Lipofectamine 2000 (Thermo Fisher Scientific). Supernatants were collected at 48 and 72 hours post-transfection and the virus was concentrated using Lenti-X concentrator solution and centrifugation, according to the manufacturer's instructions (Takara Bio, San Jose, CA). The virus was resuspended in cold PBS and the aliquots were stored at -80°C. Lentiviral titer was determined using Lenti-X GoStix, according to the manufacturer's instructions (Clontech, Mountain View, CA). Cells were infected with high titer of the lentivirus followed by selection with puromycin (0.7 μg/mL). Decreased ClpP expression in the *ClpP* KO pool in GSC923 and TS603 cells was verified by Western blot analysis.

Western blotting

Cells were lysed using RIPA buffer, and the protein concentration was measured using DC (detergent compatible) protein assay (Bio-Rad Laboratories, Hercules, CA; RRID: SCR_008426). Western blot analysis was performed as described previously (18). The following antibodies were used: IDH1 R132H (Millipore Sigma, clone HMab-1, #MABC171), ClpP (Cell Signaling, #14181), TFAM (Cell Signaling, #8076), TUFM (Thermo Fisher Scientific, PA5-27511), TSFM (Thermo Fisher Scientific, PA5-27652), NDUFS3 (Thermo Fisher Scientific, #459130), SDHA (Abcam, #ab14715), SDHB (GeneTex, GTX113833), ATF4 (Cell Signaling, #11815), phospho-AKT (S473) (Cell Signaling, #9271), phospho-mTOR (Ser2448) (Cell Signaling, #2971), phospho-4E-BP1 (Cell Signaling, # 2855), phospho-S6 (Cell Signaling, # 4857), c-PARP (Cell Signaling, #5625), GAPDH (Cell Signaling, #5174), and ACTIN (Cell Signaling, #4970).

Blue native polyacrylamide gel electrophoresis and complex I in-gel activity assay

Cells were seeded in 2D culture in the Geltrex-coated 10-cm culture plates and treated with DMSO or 25nM or 50nM TR107 for 48 hours. Cells were washed with PBS and harvested using Accutase. The cells were homogenized in the sample buffer, supplemented with 1% digitonin. After centrifugation at 20,000 g for 30 min at 4°C, the supernatant was collected. Protein concentration was measured by the DC protein assay kit (Bio-Rad) and the same amount of sample was mixed with sample buffer, 5% G-250 sample additive, and deionized water for native gel electrophoresis in dark blue cathode buffer at 150V. The gel was fixed in 40% methanol and 10% acetic acid buffer, then washed in destain buffer (8% acetic acid) until the background was washed off for visualization by the ChemiDoc Imaging system (Bio-Rad).

For complex I in-gel activity assay, the gel electrophoresis was run in light blue cathode buffer. The gel was incubated in freshly prepared complex I substrate buffer (2 mM Tris Cl, 0.1 mg/ml NADH, 2.5 mg/ml Nitrotetrazolium Blue chloride) for 20 min (19). The reaction was stopped by 10% acetic acid and the gel was washed with water for visualization by ChemiDoc Imaging system (Bio-Rad).

MitoTracker staining and super-resolution confocal live cell imaging

Cells were seeded in 2D culture in the Geltrex-coated glass slides with removable silicone chambers (ibidi) and treated with DMSO or 50nM TR107 for 24 hours. Cells were stained with MitoTracker Red CM-H2HRos (500 nM, Thermo Fisher Scientific) and Hoescht 33342 for 20 minutes at 37°C in the CO_2 incubator.

Super-resolution confocal images were collected using a Nikon SoRa super-resolution spinning disk microscope equipped with a 60x Apo TIRF oil immersion objective lens (N.A. 1.49) and Photometrics BSI sCMOS camera. Z-stack images were acquired with 0.027 μm x-y pixel size and 0.15 μm step size and post-acquisition were processed using the Denoise.ai algorithm in the Nikon Elements software (v. 5.4.1). Mitochondria were segmented using the Labkit machine learning pixel classifier in the isosurface module of the Imaris (v. 10.1.1, RRID: SCR_007370) image analysis software (Bitplane), where the volume of the individual mitochondria was measured (20). The average mitochondrial volume was calculated for both control and treated cells. In the case where the sub-cellular mitochondrial density was too high to be segmented into individual mitochondria, this mitochondrial mass was excluded from the average volume measurement by applying a volume size filter of 15 μm^3, ensuring that only individual mitochondria with a volume less than 15 μm^3 would be included in the quantitation.

Transmission electron microscope (TEM) assay

The cells were seeded in 3D culture and treated with DMSO or 50nM TR107 for 48 hours. The cells were washed with PBS and fixed in 2% paraformaldehyde, 2.5% glutaraldehyde in 0.1 M PIPES, pH7.4, for one hour and overnight at 4°C. After fixation, cells were collected by centrifugation, resuspended in quench solution containing 50mM glycine and 0.1M PIPES for 15 minutes, washed and enrobed in 2.5% low melting point agarose. Agarose containing cells were trimmed into ~1mm^3 cubes, post fixed with 1% osmium tetroxide, 0.75% potassium ferrocyanide in 0.1M PIPES at room temperature for one hour, washed with water three times, followed by en bloc staining with 1% uranyl acetate in water for one hour. Specimens were then washed and dehydrated using 30%, 50%, 70%, 90% and 100% ethanol in series, 10 minutes each. This was followed by two more changes of 100% ethanol and two more changes of 100% acetone before infiltrated with Epoxy resin (Poly/Bed812, Warrington, PA) following manufacturer's recommendation. Specimens were embedded in Epoxy resin and polymerized at 60°C overnight. Resin blocks containing cells were trimmed and sectioned using a Leica UC6 ultramicrotome

(Leica Microsystems, Inc., Bannockburn, IL). Silver colored (~70nm) ultrathin sections were collected onto 200 mesh Cu TEM grids, counterstained with uranyl acetate and lead, and examined in a Hitachi 7800 transmission electron microscope operated at 80 kV. Digital images were acquired using an AMT bottom mount camera (Nanosprint15, MKII, Advanced Microscopy Techniques, MA).

Mitochondrial DNA (mtDNA) copy number analysis

Cells were seeded in 3D culture and treated with DMSO or 25 nM TR107 for 24 hours. Genomic DNAs from cells were isolated with DNeasy Blood & Tissue kit (Qiagen, Germantown, MD). mtDNA copy number change was analyzed using Human mtDNA monitoring kit (Takara Bio USA Inc., Mountain View, CA). The relative number of copies of human mtDNA was examined by real-time PCR using two mtDNA targets (ND1, ND5). The two nuclear DNA (nDNA) targets (SLCO2B1, SERPINA1) were used as a standard. For real-time PCR reaction, Power SYBR™ Green PCR Master Mix was used (Applied Biosystems, Waltham, MA). mtDNA copy number calculation was performed according to the manufacturer's instructions.

Mitochondrial respiration and real-time ATP production assays

Mitochondria respiration and real-time ATP production were assessed by Seahorse XF Cell Mito stress test kit (Agilent) and Seahorse XF Real-Time ATP rate assay kit (Agilent, Santa Clara, CA), respectively. Briefly, cells were seeded as 2D culture at a density of 0.04 x 10^6 cells/well in the 96-well Seahorse microplates. Next day, cells were treated with DMSO or TR107 for 24 hours. Sensory cartridge was hydrated in a non-CO_2, 37°C incubator for 12–18 h prior to analysis. Medium in all wells was replaced by the XF based assay medium supplemented with 10mM glucose, 10mM sodium pyruvate and 2mM glutamine. After loading to the Seahorse XF96 analyzer (Agilent), compounds included in the Mito stress test kit (oligomycin, FCCP, and Rot/AA) or Real-Time ATP rate assay kit (oligomycin and Rot/AA) were injected according to the pre-set programs for measurement. The data were normalized to the cell count measured by Celigo Image cytometer, per manufacturer's protocol.

ROS measurement

Cells were seeded in 2D culture at 6 x 10^3 cells/well in 96-well white wall, clear bottom plates and treated with DMSO or TR107 for 48 hours. ROS was measured using ROS-Glo H_2O_2 assay kit (Promega). H_2O_2 substrate solution was added in the culture medium and incubated for 6 hours. After adding ROS-Glo detection solution and incubating for 20 minutes, luminescent signal was read by the POLARStar Optima plate reader. The data were normalized to the cell count determined by Celigo Image cytometer, per manufacturer's protocol.

Global proteomics analysis

Each cell pellet was lysed in 500µL EasyPep Lysis buffer (Thermo Fisher PN A45735) with 1X Phosphatase Inhibitor (Thermo #A32957) and universal nuclease (Thermo #88700). Protein concentration was determined by BCA method. Proteins were reduced and alkylated and digested with Trypsin/LysC, labeled with TMTpro and cleaned. Approximately 2% of the sample was saved for total protein quantification and the remaining 98% was enriched sequentially using TiO2 and IMAC. Peptides were analyzed using a Dionex U3000 RSLC in front of an Orbitrap Eclipse (Thermo) and data was processed in Proteome Discoverer 2.4. For detailed methods please see Supplemental Materials.

Ingenuity Pathways Analysis (IPA) analysis

The differential mRNA and protein expression results were uploaded into IPA and run through the core analysis algorithm to calculate a list of enriched pathways. The top ~500 genes from each cell line, based on LFC and *p*-value of .05, and significantly impacted proteins were filtered based on an absolute LFC cutoff of .4 and a *p*-value cutoff of .05 for each cell line were tested against the background user set of genes and proteins for pathway enrichment.

Colony Formation Assay

Cells were seeded at 1000 cells/well in 6-well plates and treated with DMSO or 25nM TR107 for 24 hours followed by culturing in fresh drug-free media for 2 weeks before fixation. Colonies were fixed with 4% PFA in PBS, washed, and stained with 0.5% crystal violet before counting using ImageJ software (RRID: SCR_003070).

Cell Cycle Analysis

The cells were seeded in 2D culture at $0.2x10^6$ cells/well in 6-well plates and treated with DMSO or TR107 for 8 hours, 16 hours, 1 day, 2 days, 4 days, and 6 days' time points. The cells were harvested using Accutase, washed with PBS, and fixed in 70% ethanol at −20°C. Prior to staining, the cells were washed with cold PBS and incubated with 500 µL FxCycle PI/RNase Staining Solution (#F10797, Thermo Fisher Scientific) for 30 minutes at room temperature in the dark. The data were acquired on a BD LSR Fortessa flow cytometer and analyzed using FlowJo software (RRID: SCR_008520).

Apoptosis Assays

Apoptosis was analyzed by flow cytometry using the FITC Annexin V Apoptosis Detection Kit with PI (#640914, Biolegend). Briefly, cells were seeded in 2D culture at $0.2x10^6$ cells/well in 6-well plates and treated with DMSO or TR107 for 8 hours, 16 hours, 1 day, 2 days, 4 days, and 6 days' time points. The cells were harvested using Accutase and washed with PBS. Then the cells were washed twice with Cell Staining Buffer (Biolegend), resuspended in 100 µL Annexin V binding buffer, 5 µL of FITC Annexin V, and 10 µL of PI solution. After 15-minute incubation at room temperature in the dark, 400 µL of Annexin V Binding Buffer was added, and the samples were analyzed using BD LSR Fortessa flow cytometer and FlowJo software. Unstained and single-stained samples were used to calculate compensation.

Real-time cell growth assay

Real-time cell growth was measured on the IncuCyte S3 system (Essen BioScience), which quantified cell area confluence over a period of 6 days in culture. Briefly, cells were seeded in 2D culture at $0.06x10^6$ cells/well in 12-well plates. Next day, the cells were treated with DMSO or TR107. Assay plates were imaged in the IncuCyte S3 system, under phase contrast, 10× magnification with automatic recording every 24 hours. Data were analyzed using IncuCyte software, which quantifies cell area confluence values (and standard errors for multiple well replicates) at each time point. All IncuCyte assays were performed with at least 3 replicates per condition.

BrdU Cell Proliferation Assay

The cells were seeded in 2D culture at $5x10^3$ cells/well in 96-well plates and treated with DMSO or TR107 for 8 hours, 16 hours, 24 hours, 48 hours, and 72 hours' time points. Cell proliferation was examined using the BrdU Cell Proliferation Assay Kit (Abcam, ab287841) per manufacturer's instructions.

Statistical Analysis

Statistical analyses were performed using GraphPad Prism software (version 9.3.1, San Diego, CA; RRID: SCR_002798). The data is expressed as mean ±SEM. A 2-tailed t-test was used to evaluate a difference between experimental groups. $P < 0.05$ was considered statistically significant. $*P < 0.05$, $**P < 0.01$, $***P < 0.001$.

Availability of data and materials

The global proteomics datasets generated in this study are publicly available in Gene Expression Omnibus (GEO, RRID: SCR_005012) at MassIVE Repository at MSV000095625 (Global proteomics).

RESULTS

TR107, a ClpP activator, preferentially targets IDH-mutant patient-derived glioma cells.

To examine the *in vitro* antiproliferative efficacy of TR107, multiple patient-derived glioma cell lines, including those harboring *IDH* mutations, were treated with increasing concentrations of TR107 or ONC201 for a duration of 4 days, after which time cell viability was evaluated. The mutation status of the newly identified IDH-mutant glioma cells was confirmed by Western blot (Fig. S1). ONC201(Dordaviprone), an FDA-approved ClpP activator, was used as a comparison. The sensitivity to ONC201 varied across the tested cell lines, with IC_{50} values ranging from 0.8 to 15 μM. By contrast, TR107 was markedly more potent and demonstrated IC_{50} values in the low nanomolar range in most of the cell lines, ranging from 5.5 to 99 nM, suggesting that both IDH-wildtype and IDH-mutant cells displayed a higher sensitivity to TR107 than ONC201 (Fig. 1A and 1B). Based on the overall IC_{50} trend observed in the drug response assays, treatment with either ClpP activators, TR107 or ONC201, was more effective in IDH-mutant cell lines compared with wildtype counterparts (Fig. 1A-C). To determine whether ClpP activators exert a preferential effect on IDH-mutant cells, both IDH-wildtype and IDH-mutant cells were treated with TR107 in a dose-dependent manner over 6 days to assess the long-term effects. Interestingly, dose escalation revealed that the IDH-mutant cells, TS603, was highly sensitive at concentration as low as 12.5 nM, whereas the IDH-wildtype cells, GSC923, remained viable under the same conditions (Fig. 1D). To further confirm whether IDH-mutant cells are more susceptible to TR107, isogenic IDH-mutant GBM1 cells generated by single-base gene editing were treated with increasing concentrations of TR107 over 6 days. The results consistently demonstrated that TR107 preferentially inhibited the cell viability of IDH-mutant cells at 12.5 nM, compared to their wildtype counterpart (Fig. 1E). We also evaluated the cytotoxic effects of TR107 (50 nM, 3 days) in normal human astrocytes and found minimal cytotoxicity in these cells (Fig. S2). Collectively, these findings suggest that TR107 is highly potent at nanomolar concentrations and selectively effective against IDH-mutant glioma cells.

Effect of TR107 is mitochondrial ClpP-dependent and leads to mitochondrial protein degradation.

Next, to validate that the effects on cell viability are dependent on ClpP, we examined TR107 effects using a CRISPR-Cas9 knockout system. *ClpP* was knocked out (KO) in GSC923 and TS603—representative IDH-wildtype and IDH-mutant glioma cell lines, respectively, using two independent sgRNAs targeting ClpP. *ClpP* KO pools in both GSC923 and TS603 cells exhibited a marked reduction in ClpP expression compared to the control cells (Fig. 2A). Upon treatment with TR107, the suppression of cell viability observed in control cells was nearly completely abolished in ClpP-deficient cells (Fig. 2B). These results indicate that TR107 exerts its cytotoxic effect on glioma cells in a ClpP-dependent manner.

As targeting ClpP has been shown to result in mitochondrial protein degradation, we explored the effects of TR107 on protein expression using global proteomics analysis in GSC923 and TS603 glioma cells following treatment with TR107 at 100 nM for 24 hours. The differential protein expression results were uploaded into Ingenuity pathway analysis (IPA) and a list of enriched pathways overlapped in two cell lines is shown in Fig. 2C. Mitochondrial dysfunction was the most prominent pathway with a positive z-score in both cell lines exhibiting a higher significance in TS603, an IDH-mutant cell line. Among the top downregulated pathways, OxPhos and TCA cycle II were detected in both cells with prevalence in TS603 (Fig. 2C). Interestingly, other metabolic pathways such as ketogenesis, mevalonate pathway I, superpathway of geranylgeranyldiphosphate biosynthesis, isoleucine and valine degradation pathways were more significantly dysregulated in GSC923 cells (Fig. 2C). As mitochondrial proteins were shown to be affected by TR107 in global proteomics analysis, we ran blue native polyacrylamide gel electrophoresis and complex I in-gel activity assays to examine mitochondrial respiratory chain complex. Treatment with TR107 (25 or 50 nM) for 48 hours led to a significant decrease in the expression of all complexes, especially in TS603 cells (Fig. 2D and Fig. S3). Complex I activity was also more markedly suppressed in TS603 cells at both drug concentrations, as compared to GSC923 cells, suggesting that TR107 dysregulated mitochondrial pathways of IDH-mutant type cells through specific proteins of mitochondrial complex I (Fig. 2D). To determine whether *IDH* mutation confers distinct vulnerabilities to mitochondrial disruption, we first examined the effect of the TR107 treatment on mitochondrial protein expression across IDH-mutant and IDH-wildtype glioma cells in a time-course manner including earlier time points (6h and 9h post-treatmnet) (Fig. 2E). Acute treatment at 15 nM for 2 days led to a broad reduction of multiple mitochondrial proteins in both genotypes, indicating that TR107 exerts a global impact on mitochondrial

proteostasis (Fig. 2E). In addition, we validated the change in the expression of critical proteins involved in mitochondrial transcription and translation, including transcription Factor A (TFAM; responsible for mtDNA packaging, transcription, and stability), Tu translation elongation factor (TUFM; a mitochondrial translation factors), and Ts translation elongation factor (TSFM; a mitochondrial translation factors). Some mitochondrial proteins, including TFAM and TUFM, responded to TR107 treatment at early time points, suggesting that TR107 may specifically impact mitochondrial proteostasis. Their expression was nearly eliminated following TR107 treatment in GSC923 and TS603 cells. Moreover, the expression of the Complex I protein NDUFS3 was preferentially decreased in IDH-mutant TS603 cells, while Complex II proteins, SDHA and SDHB, were also substantially reduced in both cell lines (Fig. 2E). To identify whether any component is selectively affected in the context of IDH mutation, we next performed long-term exposure tests using an isogenic cell-line pair differing only in IDH1 status. Notably, prolonged treatment resulted in a gradual decrease in TFAM levels, similar to other mitochondrial proteins such as SDHA and TUFM (Fig. 2F). This coordinated reduction suggests that TR107 broadly disrupts mitochondrial proteostasis rather than selectively affecting individual components. Consistent with this, multiple mitochondrial proteins were progressively diminished over time in both cell lines. Consequently, these findings support the idea that TR107 impairs mitochondrial function through widespread proteostatic disruption, which may contribute to the vulnerability of glioma cells to ClpP-targeting agents. Taken together, these results suggest that TR107 may trigger mitochondrial dysfunction through degradation of proteins involved in OxPhos and TCA cycle as well as mitochondrial transcription, translation processes, and amino acid metabolism.

TR107 induces a cascade of mitochondrial dysfunction in IDH-mutant glioma cells, manifested by altered mitochondrial morphology, reduced mtDNA copy number, impaired oxygen consumption, and decreased ATP production.

The mitochondria were labeled with MitoTracker and imaged using super-resolution confocal live cell imaging in GSC923 and TS603 cells treated with 50 nM of TR107 for 24 hours. TR107 treatment induced mitochondrial fragmentation and structural damage in both cell lines. In contrast, nuclei stained with Hoescht 33342 remained intact, suggesting preserved nuclear integrity following treatment (Fig. 3A). To assess whether TR107 affected mitochondrial content, quantitative analysis was performed to measure mitochondrial volume per cell in DMSO-treated

controls and TR107-treated groups (Fig. 3B). TR107 significantly reduced mitochondrial volume in both GSC923 and TS603 cells at 24 hours, suggesting that TR107 targets mitochondria and leads to their structural impairment (Fig. 3A and 3B).

To further examine mitochondrial morphology, the transmission electron microscopy (TEM) was performed. As shown in Fig. 3C, DMSO-treated control cells exhibited a high density of normal mitochondria with intact cristae (black arrows). In contrast, TR107 treatment induced marked mitochondrial alterations consistent with multiple stages of mitophagy, including vacuolization and cristae disintegration. In GSC923 cells, the presence of autophagosomes with double membranes surrounding mitochondria (orange arrows) suggested an early phase of mitophagy. Additionally, abnormal vacuolated mitochondria with disrupted cristae were frequently observed in close proximity to rough endoplasmic reticulum cisternae (red arrows). Notably, lipid droplets (yellow arrows) were detected exclusively in GSC923 cells following 48 hours of TR107 treatment. In TS603 cells, an increased number of autophagic structures containing degraded mitochondria (orange arrows) were evident, indicative of a more advanced stage of mitophagy. Severely degraded mitochondrial remnants, appearing as membrane structures devoid of cristae or cavities (red arrows), were also prominent, while mitochondria with normal morphology were largely absent. Despite these mitochondrial changes, nuclear morphology remained intact in both cell lines (blue arrows). Consistent with these observations, TR107 treatment significantly increased the dead/live cell ratio judged by visual inspection of the cellular morphology in TEM images of both GSC923 and TS603 cells, revealing a markedly higher ratio in TS603 cells (Fig. 3D).

Mitochondrial DNA (mtDNA) copy number is considered a biomarker of mitochondrial function (21). Because TR107 treatment suppressed the expression of mitochondrial transcriptional and translational factors (Fig. 2E and 2F), reduced mitochondrial volume, and impaired mitochondrial morphology (Fig. 3A-3C), we investigated whether mtDNA copy number was also affected by the treatment. Indeed, 24 hours after TR107 treatment, mtDNA copy number was significantly reduced in both GSC923 and TS603 cells with a more profound decrease observed in TS603 (Fig. 3E). Next, we evaluated the effect of TR107 on mitochondrial respiration and glycolysis in live cells using a Seahorse mito stress assay. The oxygen consumption rate (OCR) that reflects mitochondrial oxidative phosphorylation (OxPhos) was suppressed in both GSC923 and TS603 at 24 hours after TR107 treatment. The extracellular acidification rate (ECAR) that

measures glycolysis showed a slight shift to increase that appeared to be more present in GSC923 cells, compared to IDH-mutant TS603 (Fig. 3F). We then measured the ATP production rates in the real-time setting and found that TR107 significantly suppressed mitoATP levels, while increasing glycoATP in both GSC923 and TS603. However, the glycoATP increase in response to TR107 in GSC923 seemed to compensate the overall ATP production rate, as compared to a more profound decrease of total ATP in TS603 cells (Fig. 3G). These results suggest that the resulting bioenergetic stress, ATP depletion, and disruption of mitochondrial homeostasis collectively reduce the cell's ability to sustain survival pathways through mitochondrial energy metabolism, thereby enhancing cytotoxicity and promoting cell death. In other words, the metabolic collapse triggered by TR107 underlies the drug's antitumor activity .

To examine whether IDH-mutant cells are more susceptible to TR107, the isogenic GBM1 IDH-wildtype and IDH-mutant cells were used. Intriguingly, the OCR levels were suppressed in both cells with a more significant decrease in IDH-mutant cells (Fig. 3H). In contrast, the ECAR measurement revealed an increase in IDH-wildtype cells only (Fig. 3I). Furthermore, the real-time mitoATP production rate was suppressed in IDH-mutant cells, while an increase of glycoATP was detected in IDH-wt cells upon treatment. As a result, the total ATP production was affected in IDHmutant cells only (Fig. 3J). Finally, since TR107 leads to michondrial structural and functional impairment, we checked whether it also impacts ROS H_2O_2 production. Indeed, TR107 treatment led to a substantial increase in ROS H_2O_2 levels in GBM1 cells (Fig. 3K).

Overall, these results indicate that TR107 treatment triggers a series of mitochondrial impairements in IDH-mutant glioma cells, including alterations in mitochondrial morphology, mtDNA depletion, disrupted energy metabolism, diminished oxygen consumption rates and decreased ATP production.

TR107-induced cell cycle arrest and activation of apoptosis is more pronounced in IDH-mutant cells.

To investigate whether TR107-induced mitochondrial stress triggers cell cycle arrest in IDH-mutant glioma cells, the tumor cells were examined at different time points from 8 hours to 6 days after the drug treatment. As early as 16 hours, there was an increase in G0/G1 cell population detected in TS603 cells. Increase in G0/G1 and corresponding decrease in S and G2/M phases was more pronounced in TS603 IDH-mutant cells starting at day 1 of treatment, as compared to

GSC923 IDH-wildtype cells. At later time points – days 4 and 6 of treatment, a significant increase in sub-G1 cell population was detected particularly in TS603 cells (Fig. 4A), suggesting that apoptosis may occur in IDH-mutant cells after a more prolonged treatment with TR107. Overall, TR107 appears to diminish cell growth through induction of G0/G1 cell cycle arrest and suppression of DNA replication at S phase, while inducing cell death in IDH-mutant cells. Additionally, to explore the effects of TR107 on apoptosis, the AnnexinV/PI double staining was performed in live cells at different time points from 8 hours to 6 days after the drug treatment to match the cell cycle analysis. An increase in the proportion of early and late apoptotic cells was detected in TS603 cells as early as 2 days of treatment with a more substantial cell death at days 4 and 6, as compared to GSC923 cells. It is noteworthy that by day 6 of TR107 treatment, the percentage of late apoptotic cells in TS603 cells reached 96 - 97%, while it accounted only 47 - 51% in GSC923 cells treated with the same concentration of the drug (25nM or 50nM) (Fig. 4B). Taken together, these results indicate that TR107 suppresses cell viability in both IDH-wildtype and IDH-mutant cells, however, the IDH-mutant cells experience a more profound cell cycle arrest and increased cell death in response to TR107 treatment.

TR107 induces cell death in isogenic IDH-mutant glioma cells specifically through inhibition of the mTOR/4EBP1/AKT signaling pathway.

To determine whether IDH-mutant cells are more sensitive to TR107, isogenic GBM1 cells were analyzed using IncuCyte live-cell imaging. GBM1 IDH-wildtype and GBM1 IDH-mutant cells were treated with either DMSO or 15nM of TR107 and monitored over a 6-day peroid. IDH-mutant cells displayed a complete arrest in cell growth upon TR107, whereas IDH-wildtype cells continued to maintain an increase in cell confluency altough the cell growth rate was decreased compared to the DMSO-treated controls (Fig. 5A). Next, we examined cell proliferation by BrdU assay in both cells and found that IDH-mutant cells had significantly suppressed cell proliferation, compared to IDH-wildtype cells, when treated with 15 nM of TR107 for 72 hours (Fig. 5B). Finally, the Annexin V/PI double staining confirmed that IDH-mutant cells had a greater increase in the proportion of early and late apoptotic cells, as compared to IDH-wildtype cells in response to TR107, suggesting that the *IDH* mutation is associated with increased vulnerability of tumor cells to TR107 treatment (Fig. 5C).

To further investigate the molecular mechanism of TR107, we performed western blots in the isogenic GBM1 cells (Fig. 5D). Since it was shown that ONC201 inhibits AKT pathway and enhances durability of the mTOR inhibitor in breast cancer (22,23), we examined the effects of TR107 on AKT/mTOR pathway. Interestingly, p-AKT and the mTOR downstream target p-4EBP1 were elevated during the initial 1–2 days of treatment in both cell lines and remained at similar levels with continued treatment. In contrast, in IDH-mutant GBM1 cells, p-AKT, p-mTOR, and p-4EBP1 gradually declined at later time points (days 4 and 6) compared to wild-type cells, whereas cleaved PARP1 remained elevated, indicating preferential induction of apoptosis in the mutant cells (Fig. 5D). Interestingly, p-S6 (phosphorylated S6 ribosomal protein), a key downstream readout of AKT/mTOR signaling, was preferentially downregulated in IDH-mutant GBM1 cells in a time-dependent manner (Fig. 5D). These findings suggest that TR107 induces a non-canonical or rewired mTOR signaling state characterized by differential downstream substrate regulation, in which S6K/S6 signaling is attenuated despite maintained mTORC1 and 4EBP1 phosphorylation. TR107 treatment also increased cleaved PARP1 and ATF4 expression—a hallmark of mtUPR activation—in a time-dependent manner, preferentially in IDH-mutant glioma cells (Fig. 5D). This elevation was sustained during prolonged incubation, suggesting that TR107-induced ATF4 amplifies mitochondrial stress, ultimately promoting apoptosis in the IDH-mutant glioma cells persistantly. Consistent with previous reports for ONC201, our findings suggest that TR107 may similarly impact AKT/4EBP1/mTOR activity in IDH-mutant glioma cells, linking mitochondrial stress to suppression of pro-survival signaling.

ClpP agonism preferentially suppresses IDH-mutant glioma growth *in vitro*, *ex vivo*, and *in vivo*

Treatment with the ClpP agonist, TR107, significantly impaired clonogenic growth of IDH-mutant glioma cells, resulting in a marked reduction in colony number and colony size compared with DMSO-treated controls (Fig. 6A–B). Notably, the anti-proliferative effects of TR107 were significantly greater in IDH-mutant glioma cells than in IDH–wildtype counterparts under identical conditions (Fig. 6A–B). Moreover, *ex vivo* treatment of microdissected IDH-mutant glioma microtumor in a dose-dependent manner demonstrated a significant reduction in tumor cell viability following ClpP agonist exposure, further validating the efficacy of TR107 in

a physiologically relevant *ex vivo* model that preserves native tumor architecture and microenvironmental features (Fig. 6C). An orthotopic IDH-mutant glioma mouse model was established using intracranial implantation of TS603 cells to evaluate *in vivo* therapeutic efficacy (Fig. 6D). To minimize drug toxicity, we optimized TR107 dosing using multiple schedules: 8 mg/kg twice daily (BID), 8 mg/kg once daily (QD), and 4 mg/kg QD (Fig. 6D). Pharmacologic activation of ClpP by TR107 significantly extended overall survival in mice bearing IDH-mutant tumors (median survival: 45 vs. 50 days; log-rank test, $P < 0.05$) (Fig. 6E). To evaluate in vivo toxicity and clinical translation, we have performed pharmacodynamic analyses in tumor tissues following drug treatment (Fig. 6F). Specifically, we observed increased levels of apoptosis-related markers, including cleaved caspase-3 (apoptosis marker), CHOP (ER/mitochondrial stress mediator), and ATF4 (a downstream target of ClpP), in TR107-treated tumors compared to vehicle controls. In parallel, TFAM levels were reduced in tumor tissues following treatment as we observed similar effects through in vitro tests. These findings support that TR107 engages its intended mitochondrial pathway in vivo and induces mitochondrial stress–associated apoptosis. Notably, ATF4 levels were robustly and persistently elevated in tumor tissues, suggesting sustained pathway engagement and indicating that TR107 remained effective under the applied treatment schedule. This sustained ATF4 induction further supports that tumor cells were impacted through ClpP activation and its associated mitochondrial stress pathways. Additionally, only modest induction of apoptosis markers (e.g., cleaved caspase-3) was observed following the TR107 treatment schedule, which may reflect the dynamic and transient nature of apoptosis in vivo, where apoptotic cells are rapidly cleared from tumor tissues. Collectively, these results demonstrate that ClpP agonism exerts anti-tumor activity across *in vitro*, *ex vivo*, and *in vivo* models of IDH-mutant glioma.

DISCUSSION

The current study demonstrates that TR107, a novel ClpP agonist, exerts selective anti-tumor activity in IDH1-mutant glioma models, revealing a potential therapeutic vulnerability unique to the metabolic and epigenetic landscape shaped by mutant IDH1. Our findings expand the understanding of targeting IDH1-driven gliomas by suggesting that ClpP agonists like TR107 can exploit non-canonical dependencies induced by the mitochondrial dysregulation, rather than directly inhibiting the mutant IDH1 enzyme. Mechanistically, TR107 induces a cascade of mitochondrial dysregulation and robust apoptosis in IDH1-mutant glioma cells, alongside increased cell cycle arrest. The observed increase in cleaved PARP and ATF4 suggests activation of a DNA damage response (DDR), likely exacerbated by intrinsic repair defects in IDH1-mutant cells. Previous studies with ONC201 have shown that the upregulation of ATF4-ISR-DR5/TRAIL pathway by ONC201 can potentially impact the DNA damage response (DDR), possibly influencing the activity of proteins like PARP, which play crucial roles in triggering cancer cell death (24,25). Our data are consistent with these findings and raise the additional benefit that TR107 may enhance mitochondrial stress-mediated apoptosis and block tumor growth through inhibition of mTOR/AKT pathway in this context. Notably, TR107 had less cytotoxic effects in IDH-wildtype glioma cells, underscoring its potential therapeutic window and specificity. This selective vulnerability may reflect synthetic lethality arising from metabolic liabilities inherent to IDH mutation. The exact molecular target of TR107 remains under investigation, though preliminary transcriptomic and metabolomic analyses suggest involvement in mitochondrial function and oxidative phosphorylation, mTOR pathways implicated in IDH-mutant glioma tumor cell survival.

Activation of the mitochondrial protease ClpP induces mitochondrial dysfunction by degrading essential proteins involved in oxidative phosphorylation and the TCA cycle, leading to impaired ATP production and metabolic stress (22). This mitochondrial perturbation triggers energy-sensing pathways such as AMPK activation, which negatively regulate the mTOR signaling pathway (23). Consequently, ClpP activation results in inhibition of mTORC1 activity, reducing downstream anabolic processes like protein synthesis and cell proliferation. This interplay between ClpP-mediated mitochondrial stress and mTOR suppression underscores a critical mechanism by which mitochondrial-targeted therapies can exert antitumor effects through metabolic reprogramming and growth inhibition (22,26).

Unlike ONC201, which functions via a dual mechanism involving both ClpP activation and dopamine receptor (DRD2/DRD3) antagonism, TR107's anticancer activity is strictly dependent on ClpP activation. This specificity results in pronounced degradation of multiple mitochondrial proteins critical for energy metabolism, including components of the TCA cycle and oxidative phosphorylation machinery, leading to a profound impairment of mitochondrial respiration and induction of metabolic reprogramming towards glycolysis. Pharmacokinetic evaluation further revealed that TR107 possesses superior oral bioavailability and systemic exposure relative to ONC201, with a markedly higher area under the curve (AUC) and sustained plasma concentrations at comparable or lower doses (11). Importantly, the cytotoxic potency of TR107 remains robust regardless of glucose availability in the cellular environment, whereas ONC201 exhibits diminished activity under low-glucose or galactose conditions, indicating that TR107 may be less susceptible to metabolic heterogeneity within the tumor microenvironment (11). Clinically, ONC201 has progressed to FDA approval for H3K27M-mutant diffuse midline gliomas following successful phase I–III trials, where it established a favorable safety profile and promising efficacy that extends to other indications like hematological malignancies. (27,28). In contrast, TR107 is currently in the preclinical stage; however, the enhanced potency, selectivity, and pharmacokinetic advantages observed in preclinical models suggest that TR107 holds promise as a next-generation mitochondria-targeted agent with the potential for improved therapeutic outcomes. Further studies are warranted to evaluate the translational potential of TR107, including safety assessments and clinical trial evaluation.

Our findings reveal a significant link between glucose uptake and mTOR pathway activity in IDH-mutant tumors, which is further disrupted by pharmacologic activation of the mitochondrial protease ClpP. *IDH* mutations are known to rewire cellular metabolism, reducing glycolytic flux and glucose uptake through the accumulation of 2-hydroxyglutarate (2-HG) (29,30,31). This metabolic reprogramming suppresses mTOR signaling, reflecting a cellular adaptation to altered nutrient availability and reduced biosynthetic demands. Importantly, treatment with a ClpP activator in IDH-mutant tumor models further exacerbated mitochondrial dysfunction, leading to a marked decrease in glucose uptake and a profound inhibition of mTOR signaling. Rather than restoring metabolic homeostasis, ClpP activation destabilized mitochondrial proteostasis, triggering mitochondrial stress and ultimately inducing tumor cell death. These results suggest that IDH-mutant cells, already metabolically compromised, are particularly

vulnerable to additional mitochondrial insults. This synergistic vulnerability underscores a potential therapeutic strategy: combining metabolic stressors such as ClpP activation with inhibitors of mTOR or glucose metabolism may selectively target IDH-mutant tumors. Overall, our data highlight ClpP as a promising pro-apoptotic target that exploits the metabolic fragility of IDH-mutant tumors by decoupling mitochondrial function from nutrient signaling pathways like mTOR.

Importantly, while our data suggest potential crosstalk between mitochondrial stress induced by TR107 and survival signaling pathways such as PI3K/AKT/mTOR, these findings should be interpreted with caution. Although pathway modulation was observed in our experimental models, our current study does not definitively establish a functional requirement or synergistic interaction between PI3K/AKT/mTOR inhibition and TR107-mediated cytotoxicity. Therefore, the therapeutic implications of combining TR107 with PI3K/AKT/mTOR inhibitors remain speculative at this stage. It is possible that the observed signaling changes reflect adaptive or compensatory responses to mitochondrial dysfunction rather than actionable vulnerabilities that enhance drug efficacy. Future studies may be required to determine whether inhibition of PI3K/AKT/mTOR signaling functionally enhances TR107 activity and contributes to durable antitumor responses.

Although ClpP agonists such as ONC201 and TR107 exhibited consistent anti-tumor activity across multiple experimental platforms (9,32), the absence of a significant improvement in overall survival in the orthotopic glioma model may be result of unoptimized dosing strategies (33). Specifically, achieving the optimal therapeutic index likely requires holding plasma concentrations above a critical threshold for a sustained duration (time-dependent efficacy), while avoiding undue peak concentrations (CMax) that drive toxicity (34). Pharmacologic activation of ClpP primarily induces mitochondrial proteostatic stress and metabolic reprogramming, which may lead to cytostatic growth suppression rather than rapid cytotoxicity. In the context of aggressive intracranial tumor growth, such cytostatic effects may be insufficient to delay the onset of lethal neurological symptoms that define survival endpoints in orthotopic glioma models. Moreover, IDH-mutant glioma cells exhibit metabolic plasticity and adaptive stress response pathways that may partially compensate for ClpP-mediated mitochondrial disruption *in vivo*, thereby limiting durable tumor regression. These adaptive responses, while not fully captured in short-term *in vitro* or *ex vivo* assays, may blunt long-term therapeutic impact in vivo. Notably,

ATF4 levels were robustly and persistently elevated in tumor tissues, suggesting sustained pathway engagement and indicating that TR107 remained biologically active under the applied treatment schedule. This sustained ATF4 induction supports ongoing activation of ClpP-associated mitochondrial stress responses in tumor cells. Due to institutional animal protocol requirements, tumor tissues were collected at the experimental endpoint, approximately 10 days after the final drug administration. Consequently, tissue harvesting may not have captured the peak window of apoptotic signaling. Given the transient nature of apoptosis and the rapid clearance of apoptotic cells in vivo, the modest levels of cleaved caspase-3 observed may underestimate the true extent of earlier treatment-induced cell death. Together, our findings suggest that ClpP agonists may be more effective as part of combination strategies designed to exploit mitochondrial stress or block compensatory survival pathways in more specific tumor types, rather than as monotherapies in regular orthotopic glioma settings. Additionally, our findings highlight the therapeutic potential of highly selective ClpP agonists like TR-107 as mitochondrial disruptors, potentially overcoming limitations associated with ONC201's dual-target mechanism and metabolic sensitivity, and opening new avenues for targeting mitochondrial vulnerabilities in cancer.

Acknowledgements: This research was supported by the Intramural Research Program of the National Institutes of Health (NIH). The contributions of the NIH authors are considered Works of the United States Government. The findings and conclusions presented in this paper are those of the authors and do not necessarily reflect the views of the NIH or the U.S. Department of Health and Human Services.

Funding support: This research was supported by the Intramural Research Program of the National Institutes of Health and Lasker Clinical Research Scholar Program.

Conflict of Interest Statement: The authors declare no potential conflicts of interest.

Authors' contributions: Conceptualization, data curation, formal analysis, validation, investigation, visualization, methodology, writing–original draft: O.K, J.J., Formal analysis, validation, investigation, visualization, methodology: S.S., G.Y., Q.L., R-C.H., M.J.K., B.T., R.H., M.Z., T.A., M.C., T.S.G Bioinformatic analysis: Z.S. *In vivo* experiments: O.K., J.J., Q.L., P.L., M.Z., H.W., M.C, T.S.G. Critical resources: R.C., L.M.G., E.J.I. Manuscript review and editing: O.K., J.J., S.S., G.Y., Z.S., Q.L., P.L., M.C., T.S.G, Z.L., J.W. Conceptualization, resources, data curation, supervision, funding acquisition, manuscript review and editing: J.W.

REFERENCES

1. Luo Y, Ma J, Lu W. The Significance of Mitochondrial Dysfunction in Cancer. Int J Mol Sci 2020;21
2. Newmeyer DD, Ferguson-Miller S. Mitochondria: releasing power for life and unleashing the machineries of death. Cell 2003;112:481-90
3. Nouri K, Feng Y, Schimmer AD. Mitochondrial ClpP serine protease-biological function and emerging target for cancer therapy. Cell Death Dis 2020;11:841
4. Mabanglo MF, Bhandari V, Houry WA. Substrates and interactors of the ClpP protease in the mitochondria. Curr Opin Chem Biol 2022;66:102078
5. Ishizawa J, Zarabi SF, Davis RE, Halgas O, Nii T, Jitkova Y, et al. Mitochondrial ClpP-Mediated Proteolysis Induces Selective Cancer Cell Lethality. Cancer Cell 2019;35:721-37 e9
6. Bonner ER, Waszak SM, Grotzer MA, Mueller S, Nazarian J. Mechanisms of imipridones in targeting mitochondrial metabolism in cancer cells. Neuro Oncol 2021;23:542-56
7. Graves PR, Aponte-Collazo LJ, Fennell EMJ, Graves AC, Hale AE, Dicheva N, et al. Mitochondrial Protease ClpP is a Target for the Anticancer Compounds ONC201 and Related Analogues. ACS Chem Biol 2019;14:1020-9
8. Venneti S, Kawakibi AR, Ji S, Waszak SM, Sweha SR, Mota M, et al. Clinical Efficacy of ONC201 in H3K27M-Mutant Diffuse Midline Gliomas Is Driven by Disruption of Integrated Metabolic and Epigenetic Pathways. Cancer Discov 2023;13:2370-93
9. Greer YE, Hernandez L, Fennell EMJ, Kundu M, Voeller D, Chari R, et al. Mitochondrial Matrix Protease ClpP Agonists Inhibit Cancer Stem Cell Function in Breast Cancer Cells by Disrupting Mitochondrial Homeostasis. Cancer Res Commun 2022;2:1144-61
10. Greer YE, Porat-Shliom N, Nagashima K, Stuelten C, Crooks D, Koparde VN, et al. ONC201 kills breast cancer cells in vitro by targeting mitochondria. Oncotarget 2018;9:18454-79
11. Fennell EMJ, Aponte-Collazo LJ, Wynn JD, Drizyte-Miller K, Leung E, Greer YE, et al. Characterization of TR-107, a novel chemical activator of the human mitochondrial protease ClpP. Pharmacol Res Perspect 2022;10:e00993
12. Yan H, Parsons DW, Jin G, McLendon R, Rasheed BA, Yuan W, et al. IDH1 and IDH2 mutations in gliomas. N Engl J Med 2009;360:765-73
13. Turcan S, Rohle D, Goenka A, Walsh LA, Fang F, Yilmaz E, et al. IDH1 mutation is sufficient to establish the glioma hypermethylator phenotype. Nature 2012;483:479-83

14. Grassian AR, Parker SJ, Davidson SM, Divakaruni AS, Green CR, Zhang X, et al. IDH1 mutations alter citric acid cycle metabolism and increase dependence on oxidative mitochondrial metabolism. Cancer Res 2014;74:3317-31
15. Ishizawa J, Zarabi SF, Davis RE, Halgas O, Nii T, Jitkova Y, et al. Mitochondrial ClpP-Mediated Proteolysis Induces Selective Cancer Cell Lethality. Cancer Cell 2019;35:721-37 e9
16. Giarrizzo M, LaComb JF, Patel HR, Reddy RG, Haley JD, Graves LM, et al. TR-107, an Agonist of Caseinolytic Peptidase Proteolytic Subunit, Disrupts Mitochondrial Metabolism and Inhibits the Growth of Human Colorectal Cancer Cells. Mol Cancer Ther 2024;23:1761-78.
17. Chari R, Yeo NC, Chavez A, Church GM. sgRNA Scorer 2.0: A Species-Independent Model To Predict CRISPR/Cas9 Activity. ACS Synth Biol 2017;6:902-4
18. Kim O, Butler M, Sergi Z, Robey RW, Zhang M, Chari R, et al. Combined inhibition of topoisomerase I and poly(ADP-ribose) polymerase: A synergistic therapeutic strategy for glioblastoma with phosphatase and tensin homolog deficiency. Neurooncol Adv 2023;5:vdad102
19. Jha P, Wang X, Auwerx J. Analysis of Mitochondrial Respiratory Chain Supercomplexes Using Blue Native Polyacrylamide Gel Electrophoresis (BN-PAGE). Curr Protoc Mouse Biol 2016;6:1-14
20. Arzt M , Deschamps J , Schmied C , Pietzsch T , Schmidt D , Tomancak P , et al. LABKIT: labeling and segmentation toolkit for big image data. Front Comput Sci 2022;4:777728.
21. Castellani CA, Longchamps RJ, Sun J, Guallar E, Arking DE. Thinking outside the nucleus: Mitochondrial DNA copy number in health and disease. Mitochondrion 2020;53:214-23
22. Armenise D, Baldelli OM, Liturri A, Cavallaro G, Fortuna CG, Ferorelli S, et al. Mitochondrial Protease ClpP: Cancer Marker and Drug Target. Pharmaceuticals (Basel) 2025;18
23. Garza-Lombo C, Schroder A, Reyes-Reyes EM, Franco R. mTOR/AMPK signaling in the brain: Cell metabolism, proteostasis and survival. Curr Opin Toxicol 2018;8:102-10
24. Kline CL, Van den Heuvel AP, Allen JE, Prabhu VV, Dicker DT, El-Deiry WS. ONC201 kills solid tumor cells by triggering an integrated stress response dependent on ATF4 activation by specific eIF2alpha kinases. Sci Signal 2016;9:ra18
25. Parker CS, Zhou L, Prabhu VV, Lee S, Miner TJ, Ross EA, et al. ONC201/TIC10 plus TLY012 anti-cancer effects via apoptosis inhibitor downregulation, stimulation of integrated stress response and death receptor DR5 in gastric adenocarcinoma. Am J Cancer Res 2023;13:6290-312

26. Nandha SR, Patwardhan RS, Sharma D, Sandur SK, Checker R. Targeting mitochondrial proteases CLPP and LONP1 via disruption of mitochondrial redox homeostasis induces proteotoxic stress and suppresses tumor progression. Cell Commun Signal 2025;23:393
27. Arrillaga-Romany I, Gardner SL, Odia Y, Aguilera D, Allen JE, Batchelor T, et al. ONC201 (Dordaviprone) in Recurrent H3 K27M-Mutant Diffuse Midline Glioma. J Clin Oncol 2024;42:1542-52
28. Gardner SL, Tarapore RS, Allen J, McGovern SL, Zaky W, Odia Y, et al. Phase I dose escalation and expansion trial of single agent ONC201 in pediatric diffuse midline gliomas following radiotherapy. Neurooncol Adv 2022;4:vdac143
29. Choate KA, Pratt EPS, Jennings MJ, Winn RJ, Mann PB. IDH Mutations in Glioma: Molecular, Cellular, Diagnostic, and Clinical Implications. Biology (Basel) 2024;13
30. Fack F, Tardito S, Hochart G, Oudin A, Zheng L, Fritah S, et al. Altered metabolic landscape in IDH-mutant gliomas affects phospholipid, energy, and oxidative stress pathways. EMBO Mol Med 2017;9:1681-95
31. Batsios G, Viswanath P, Subramani E, Najac C, Gillespie AM, Santos RD, et al. PI3K/mTOR inhibition of IDH1 mutant glioma leads to reduced 2HG production that is associated with increased survival. Sci Rep 2019;9:10521
32. Chen B, Sun M, Zhang C, Huang Q, Teng D, Hu L, et al. Discovery of CLPP-1071 as an Exceptionally Potent and Orally Efficacious Human ClpP Activator with Strong In Vivo Antitumor Activity. J Med Chem 2024;67:21009-29
33. Bucher RW, Graves LM, Bartlett DW. Dose Optimization of ClpP Agonists Using an In Vitro Microfluidic Perfusion Platform and In Silico Pharmacokinetic-Pharmacodynamic Modeling. AAPS J 2025;27:109
34. Evans DM, Fang J, Silvers T, Delosh R, Laudeman J, Ogle C, et al. Exposure time versus cytotoxicity for anticancer agents. Cancer Chemother Pharmacol 2019;84:359-71

FIGURE LEGENDS

Figure 1. TR107, a ClpP activator, preferentially targets IDH mutant patient-derived glioma cells. (A-C) The dose-response curves of ONC201 and TR107 in IDHwt and IDHmut patient-derived glioma cell lines treated with increasing drug concentrations for 96 hours. (D) Percentage of viable cells in IDHwt GSC923 and IDHmut TS603 cells treated with the increasing concentrations of TR107 for 6 days. The data is presented as viable/total cells (%) per each drug concentration. Each p-value was calculated for treatment versus control. *$p < 0.05$, **$p < 0.01$, ***$p < 0.001$. (E) Percentage of viable cells in isogenic GBM1 cells and GBM1-IDHmut treated with the increasing concentrations of TR107 for 6 days. The data is presented as viable/total cells (%) per each drug concentration. Each p-value was calculated for treatment versus control. *$p < 0.05$, **$p < 0.01$, ***$p < 0.001$.

Figure 2. Effect of TR107 is mitochondrial ClpP-dependent and its treatment leads to mitochondrial protein degradation. (A) Protein expression of ClpP in Control and *ClpP* KO cells. (B) The dose–response curves for TR107 in GSC923 and TS603 cells after *ClpP* KO treated with increasing drug concentrations for 72 hours. (C) TOP 10 altered pathways overlapped in IPA analysis using global proteomics data from GSC923 and TS603 cells treated with 100 nM of TR107 for 24 hours. (D) Blue native gel staining of the mitochondrial complexes and complex I in-gel activity assay in GSC923 and TS603 cells treated with DMSO or 25 nM/50 nM TR107 for 48 hours. (E) Western blot analysis of mitochondrial proteins such as TFAM, TUFM, TSFM, NDUFS3, SDHA, SDHB, and TOM20, ATF4, and ACTIN in GSC923 and TS603 cells treated with DMSO or 15 nM of TR107 for 6, 9, 24, and 48 hours. (F) Western blot analysis of SDHA, TSFM, TFAM, IDH R132H, and ACTIN proteins in GBM1-wt and GBM1-IDHmut cells (clone #49) treated with 15 nM TR107 on 0, 1, 2, 4, and 6 days.

Figure 3. TR107 induces a cascade of mitochondrial dysfunction in IDH-mutant glioma cells, manifested byaltered mitochondrial morphology, reduced mtDNA copy number, impaired oxygen comsumption, and decreased ATP production. (A-B) MitoTracker labeling of mitochondria (red) and Hoescht 33342 nuclear staining (blue) in GSC923 and TS603 cells treated

with DMSO or 50 nM TR107 for 24 hours. Mitochondrial volume was calculated in 20 cells per each condition and normalized to DMSO control in each cell line. (C) Representative TEM images of GSC923 and TS603 cells treated with DMSO or 50 nM TR107 for 48 hours. (D) The number of dead and live cells was counted in at least 10 fields of view per each condition using TEM (at least 100 live cells in total per sample), and the dead/live cells ratio was calculated. The data is presented as values normalized to DMSO control in each cell line. (E) mtDNA copy number detected by real-time PCR in GSC923 and TS603 cells treated with DMSO or 25 nM TR107 for 24 hours. (F) Energy phenotype plot showing OCR and ECAR levels in GSC923 and TS603 cells treated with DMSO or 25nM of TR107 for 24 hours. (G) Real-time ATP production in GSC923 and TS603 cells treated with DMSO or 25nM TR107 for 24 hours. (H) OCR levels in GBM1-IDHwt and GBM1-IDHmut cells treated with DMSO or 15nM TR107 for 24 hours. The data is presented as values normalized to DMSO control in each cell line. (I) ECAR levels in GBM1-IDHwt and GBM1-IDHmut cells treated with DMSO or 15nM TR107 for 24 hours. The data is presented as values normalized to DMSO control in each cell line. (J) Real-time ATP production in GBM1-IDHwt and GBM1-IDHmut cells treated with DMSO or 15nM TR107 for 24 hours. (K) ROS H_2O_2 levels in GBM1-IDHwt and GBM1-IDHmut cells treated with DMSO or 15nM TR107 for 48 hours.

Figure 4. TR107-induced cell cycle arrest and apoptosis are more pronounced in IDH-mutant cells. (A) Cell cycle analysis (n=3) performed by flow cytometry in GSC923 and TS603 cells treated with 25nM/50nM TR107 for 8 hours, 16 hours, 1 day, 2 days, 4 days, and 6 days. Each p-value was calculated for treatment versus control. *$p < 0.05$, **$p < 0.01$, ***$p < 0.001$. (B) Flow cytometry analysis (n=3) of GSC923 and TS603 cells by double staining with Annexin V and PI after treatment with 25nM/50nM TR107 for 8 hours, 16 hours, 1 day, 2 days, 4 days, and 6 days. Apoptosis fraction includes early (Annexin V+, PI−) and late apoptosis (Annexin V+, PI+). Necrosis was measured as Annexin V− and PI+. Each p-value was calculated for treatment versus control. *$p < 0.05$, **$p < 0.01$, ***$p < 0.001$.

Figure 5. TR107 induces apoptotic cell death in isogenic IDH-mutant glioma cells specifically through inhibiting of mTOR/4EBP1/AKT signaling pathway. (A) Area of confluence was measured every 24 hours by IncuCyte live-cell imaging in GBM1-wt and GBM1-IDHmut cells

treated with DMSO or 15nM TR107 over 6 days. The data were normalized to the treatment start point (0 hours) in each cell line. (B) BrdU cell proliferation was examined at baseline, 8, 16, 24, 48, and 72 hours' time points in GBM1-wt and GBM1-IDHmut cells treated with DMSO or 15nM TR107. The data were normalized to DMSO control in each cell line. (C) Flow cytometry analysis of GBM1-wt and GBM1-IDHmut cells using double staining with Annexin V and PI after treatment with 15nM of TR107 for 72 hours. Apoptosis fraction includes early (Annexin V+, PI−) and late apoptosis (Annexin V+, PI+). Necrosis was measured as Annexin V−, PI+. (D) Western blot analysis of p-mTOR, mTOR, p-AKT (S473), AKT, p-S6, p-4EBP1, c-PARP1, ATF4 and GAPDH proteins in GBM1-wt and GBM1-IDHmut cells treated with 15 nM TR107 on 0, 1, 2, 4, and 6 days.

Figure 6. ClpP agonism preferentially suppresses IDH-mutant glioma growth in *vitro, ex vivo*, and *in vivo*. (A) Colony formation assay in GSC923 and TS603 cells following treatment with 25nM TR107 for 72 hours, after which cellswere cultured in drug-free medium for 2 weeks. Colony formation was calculated by Image J and normalized to DMSO in each cell line. (B). Colony formation assay in GBM1-wt and GBM1-IDHmut cells treated with DMSO or 15nM TR107 for 24 hours followed by a drug-free culture for 2 weeks. Colony formation was calculated by Image J and normalized to DMSO in each cell line. (C) *Ex vivo* cell viability assay was performed in microdissected tumor cuboids from IDH-mutant glioma patient samples after 3-day treatment with 100 nM TR107 in duplicate. (D) Therapeutic schedule. (E) Kaplan-Meier survival curves of IDH-mutant orthotopic patient derived-xenograft mouse model treated with TR107 or vehicle control. Mice in each treatment arm were observed for survival up to 60 days. (F) Tumor samples were collected from each group (vehicle: mice #747 and #761 at Days 49 and 52; treatment: mice #741, #759, and #760 at Days 52, 53, and 52, respectively), followed by Western blot analysis of c-Caspase-3, TFAM, ATF4, CHOP, TOM20, and ACTIN.

Figure 1.

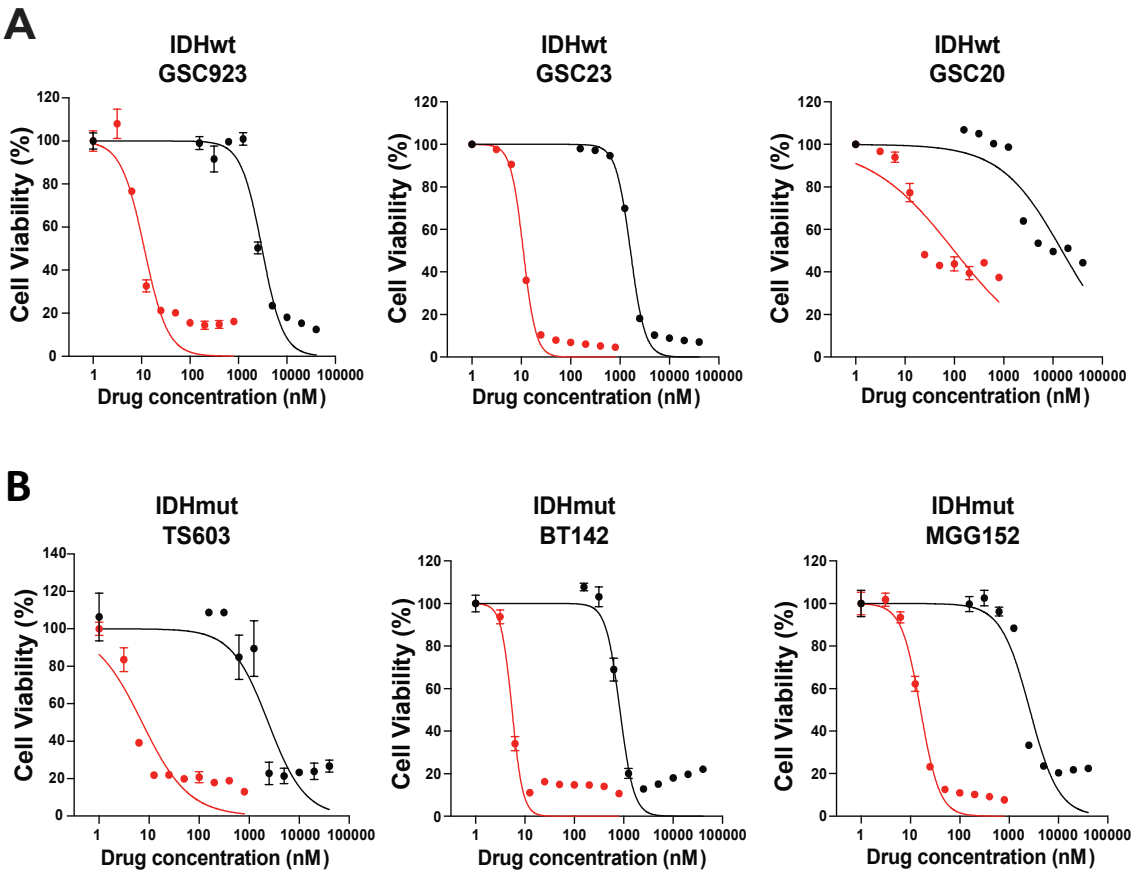

C 4 days treatment

ONC201

TR107

Cell line	IC50 (nM)	
	ONC201	TR107
GSC923	3055	11.4
GSC23	1622	11
GSC20	15155	99
TS603	2413	7.2
BT142	833.6	5.5
MGG152	2622	16

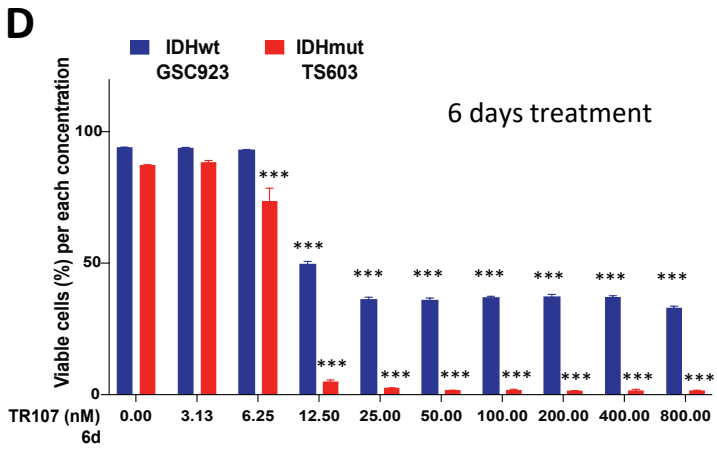

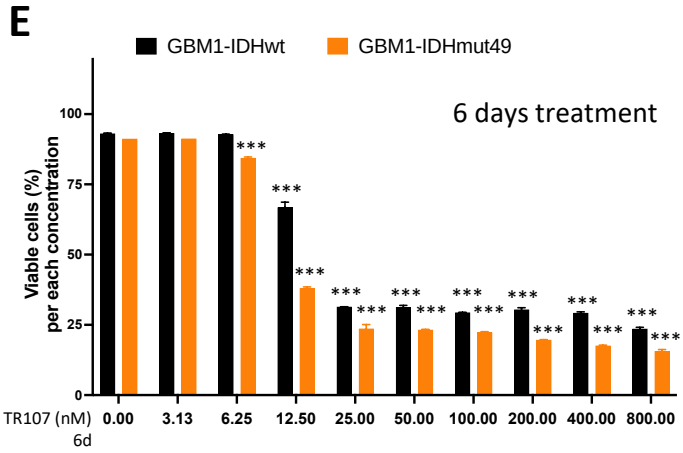

Figure 2.

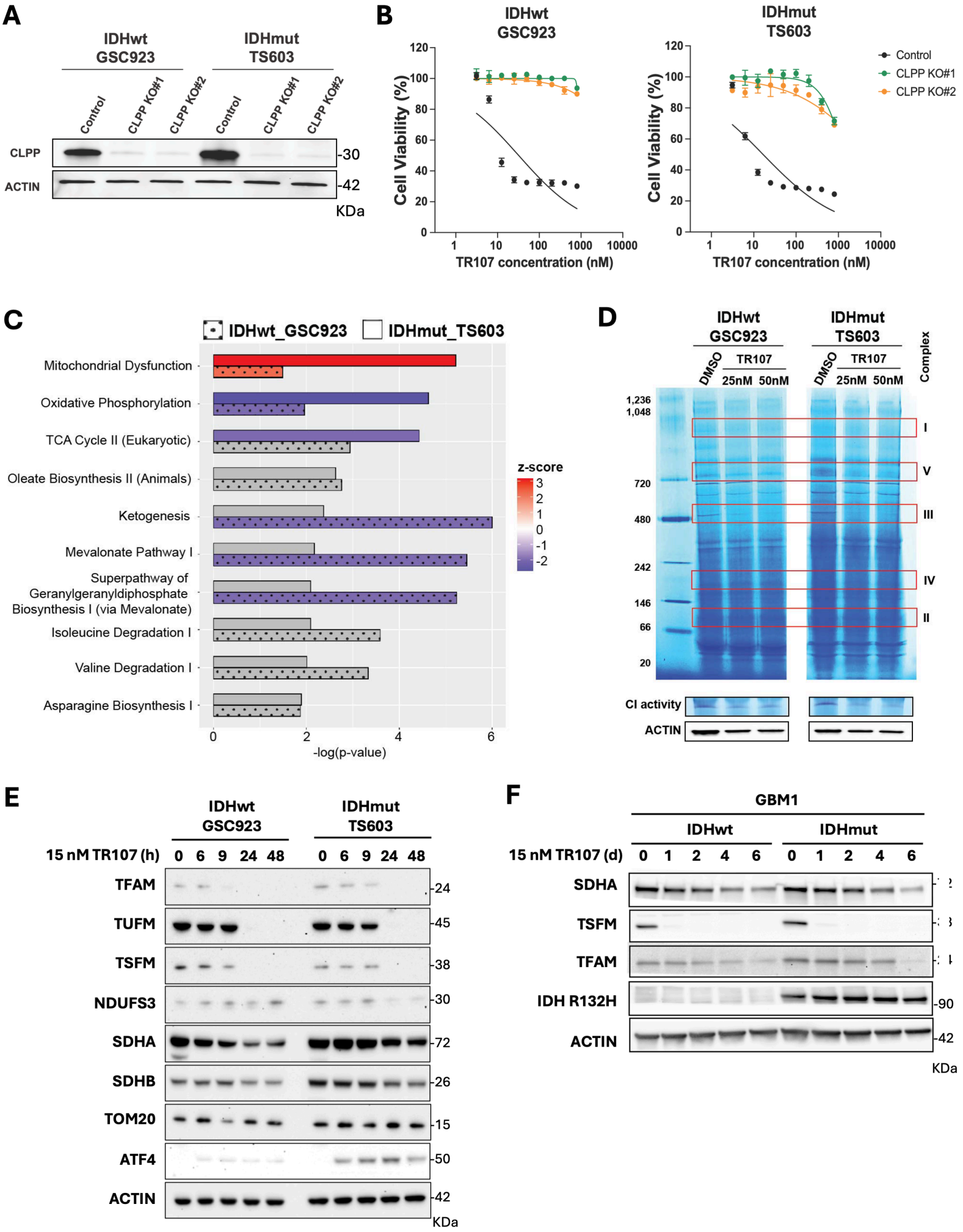
A
IDHwt GSC923
IDHmut TS603
Control
CLPP KO#1
CLPP KO#2
CLPP
ACTIN
-30
-42
KDa
B
IDHwt GSC923
IDHmut TS603
Cell Viability (%)
TR107 concentration (nM)
Control
CLPP KO#1
CLPP KO#2
C
IDHwt_GSC923
IDHmut_TS603
Mitochondrial Dysfunction
Oxidative Phosphorylation
TCA Cycle II (Eukaryotic)
Oleate Biosynthesis II (Animals)
Ketogenesis
Mevalonate Pathway I
Superpathway of Geranylgeranyldiphosphate Biosynthesis I (via Mevalonate)
Isoleucine Degradation I
Valine Degradation I
Asparagine Biosynthesis I
z-score
-log(p-value)
D
IDHwt GSC923
IDHmut TS603
DMSO
TR107
25nM
50nM
Complex
I
V
III
IV
II
CI activity
ACTIN
E
IDHwt GSC923
IDHmut TS603
15 nM TR107 (h)
TFAM
TUFM
TSFM
NDUFS3
SDHA
SDHB
TOM20
ATF4
ACTIN
KDa
F
GBM1
IDHwt
IDHmut
15 nM TR107 (d)
SDHA
TSFM
TFAM
IDH R132H
ACTIN
KDa

Figure 3.

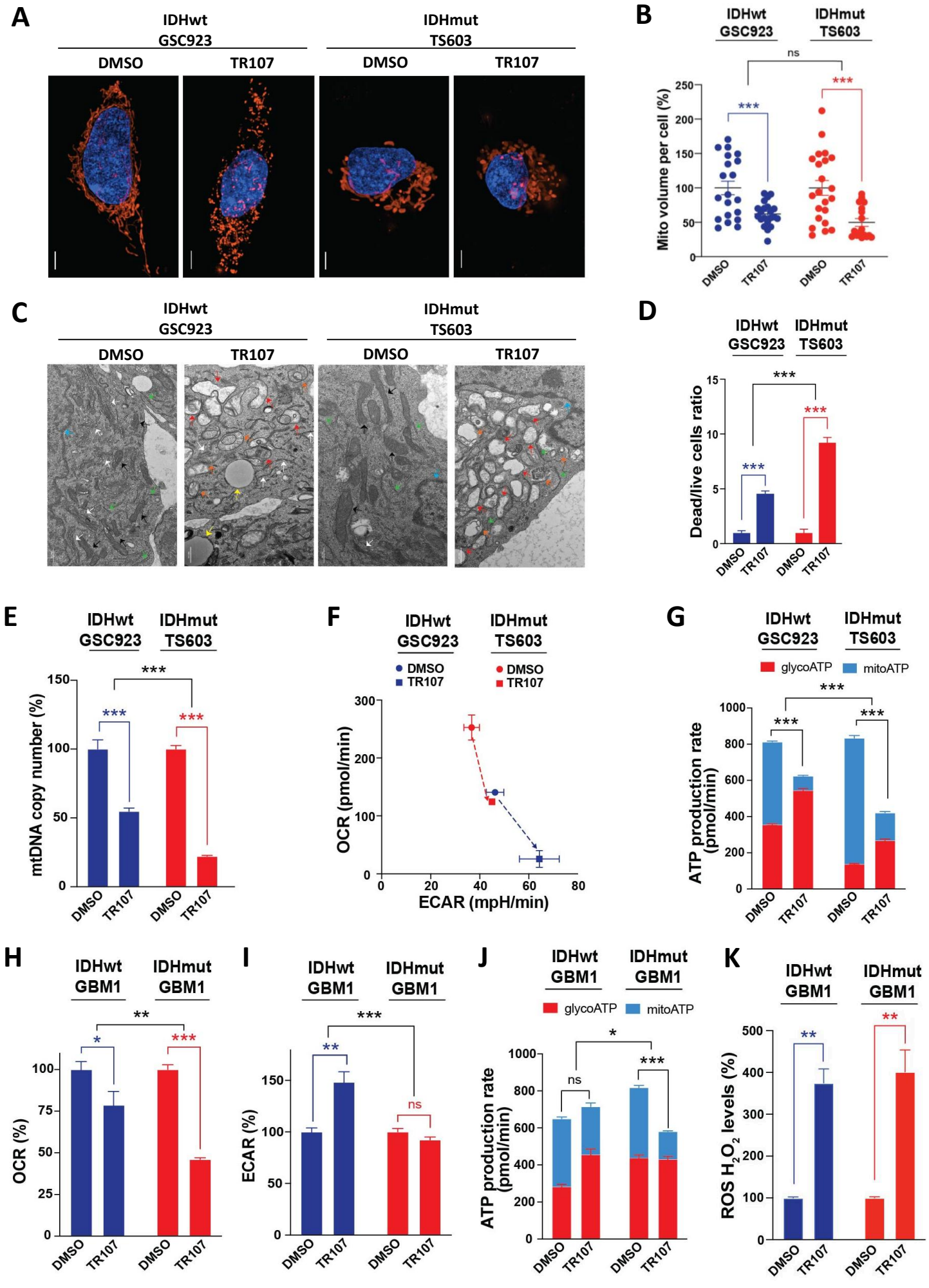
A
IDHwt GSC923
IDHmut TS603
DMSO
TR107
DMSO
TR107
B
IDHwt GSC923
IDHmut TS603
ns
***
***
Mito volume per cell (%)
250
200
150
100
50
0
DMSO
TR107
DMSO
TR107
C
IDHwt GSC923
IDHmut TS603
DMSO
TR107
DMSO
TR107
D
IDHwt GSC923
IDHmut TS603
***
***
***
Dead/live cells ratio
15
10
5
0
DMSO
TR107
DMSO
TR107
E
IDHwt GSC923
IDHmut TS603
***
***
***
mtDNA copy number (%)
150
100
50
0
DMSO
TR107
DMSO
TR107
F
IDHwt GSC923
IDHmut TS603
DMSO
TR107
DMSO
TR107
OCR (pmol/min)
300
200
100
0
0
20
40
60
80
ECAR (mpH/min)
G
IDHwt GSC923
IDHmut TS603
glycoATP
mitoATP
***
***
***
ATP production rate (pmol/min)
1000
800
600
400
200
0
DMSO
TR107
DMSO
TR107
H
IDHwt GBM1
IDHmut GBM1
**
*
***
OCR (%)
100
75
50
25
0
DMSO
TR107
DMSO
TR107
I
IDHwt GBM1
IDHmut GBM1
***
**
ns
ECAR (%)
150
100
50
0
DMSO
TR107
DMSO
TR107
J
IDHwt GBM1
IDHmut GBM1
glycoATP
mitoATP
*
ns
***
ATP production rate (pmol/min)
1000
800
600
400
200
0
DMSO
TR107
DMSO
TR107
K
IDHwt GBM1
IDHmut GBM1
**
**
ROS H_2O_2 levels (%)
500
400
300
200
100
0
DMSO
TR107
DMSO
TR107

Figure 4.

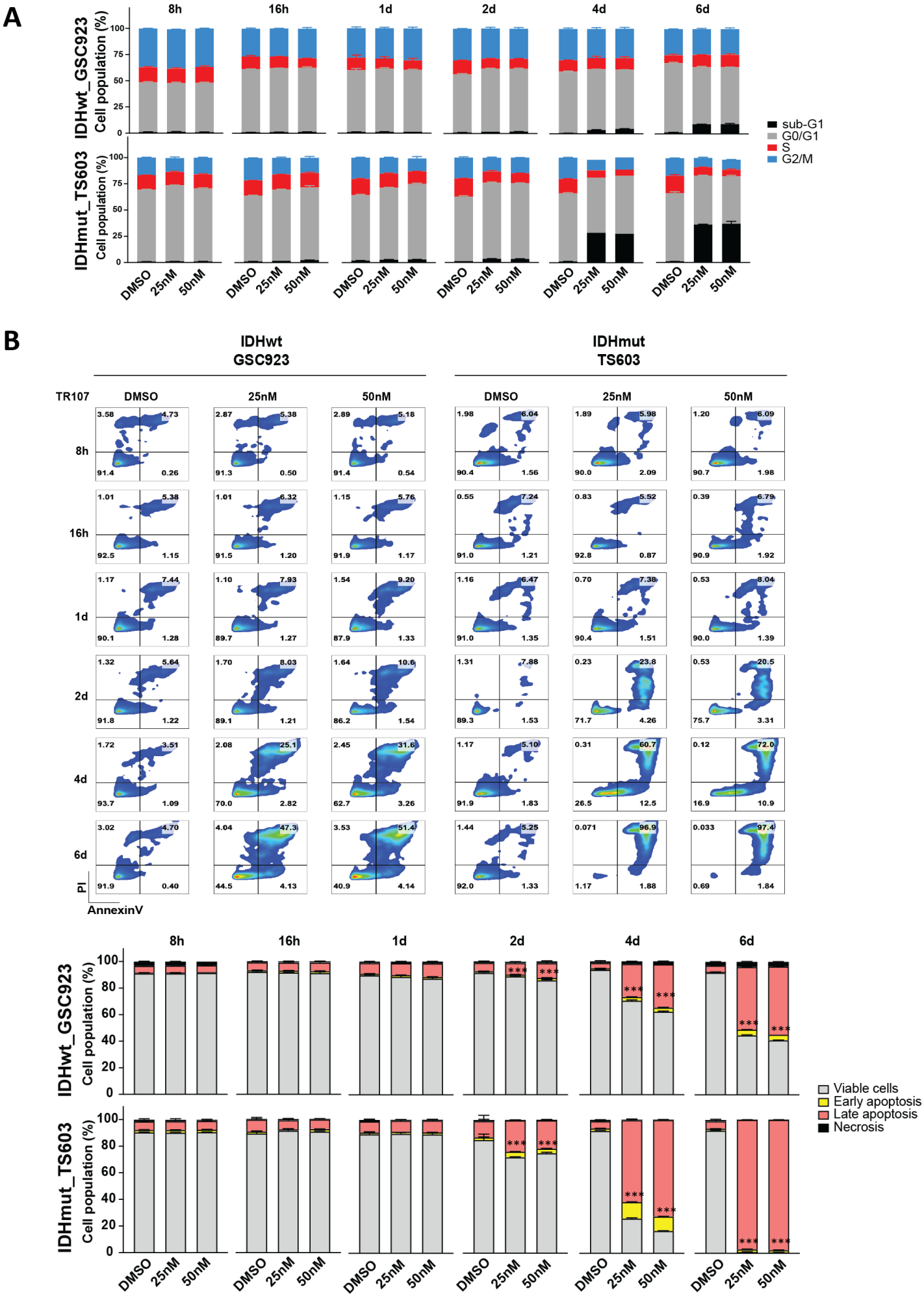
A
8h
16h
1d
2d
4d
6d
IDHwt_GSC923
IDHmut_TS603
Cell population (%)
sub-G1
G0/G1
S
G2/M
DMSO
25nM
50nM
B
IDHwt
GSC923
IDHmut
TS603
TR107
PI
AnnexinV
Viable cells
Early apoptosis
Late apoptosis
Necrosis

Figure 5.

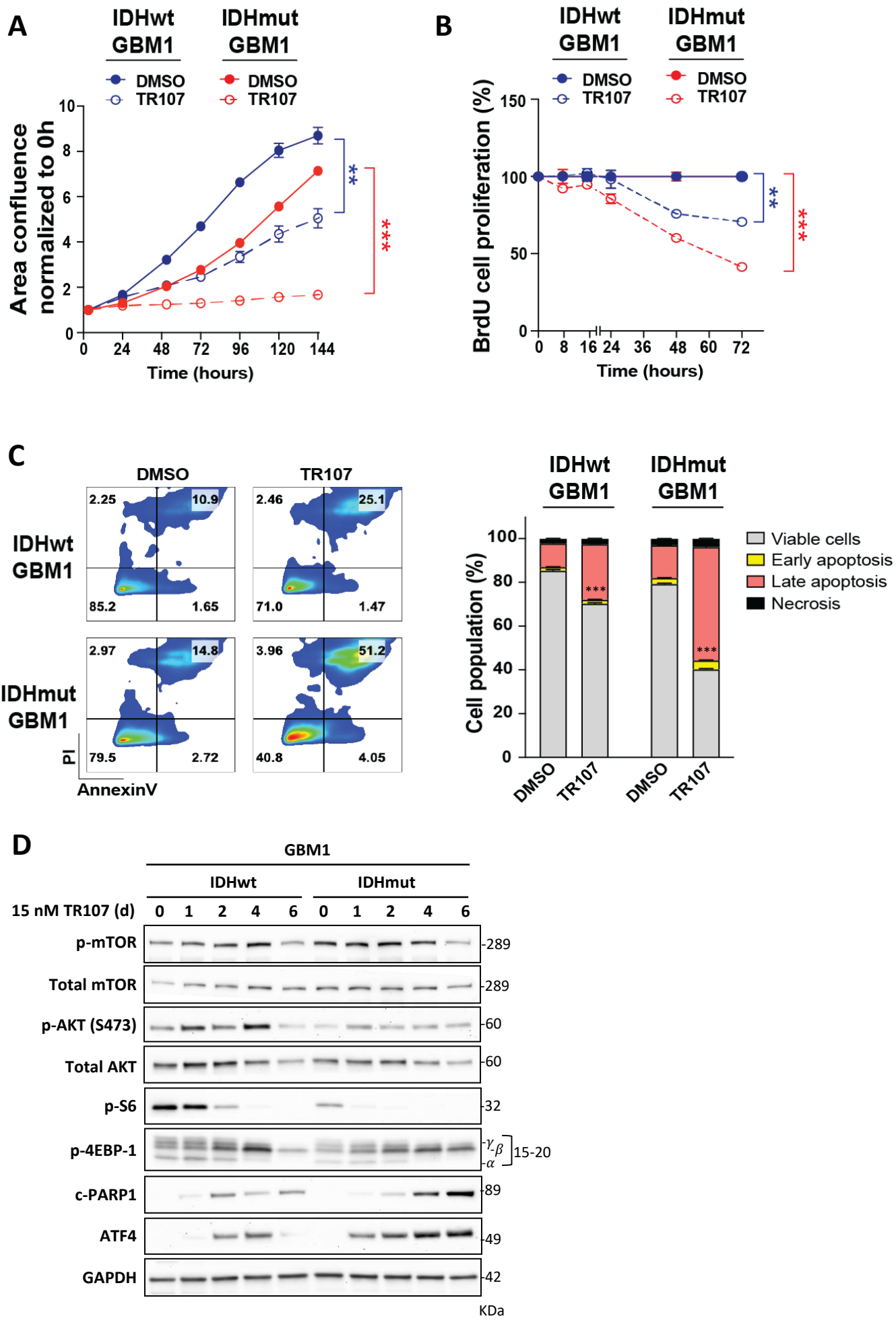
A
IDHwt GBM1
IDHmut GBM1
DMSO
TR107
Area confluence normalized to 0h
Time (hours)
B
BrdU cell proliferation (%)
Time (hours)
C
DMSO
TR107
IDHwt GBM1
IDHmut GBM1
2.25
10.9
85.2
1.65
2.46
25.1
71.0
1.47
2.97
14.8
79.5
2.72
3.96
51.2
40.8
4.05
PI
AnnexinV
Cell population (%)
Viable cells
Early apoptosis
Late apoptosis
Necrosis
D
GBM1
IDHwt
IDHmut
15 nM TR107 (d)
0 1 2 4 6 0 1 2 4 6
p-mTOR
Total mTOR
p-AKT (S473)
Total AKT
p-S6
p-4EBP-1
c-PARP1
ATF4
GAPDH
KDa

Figure 6.

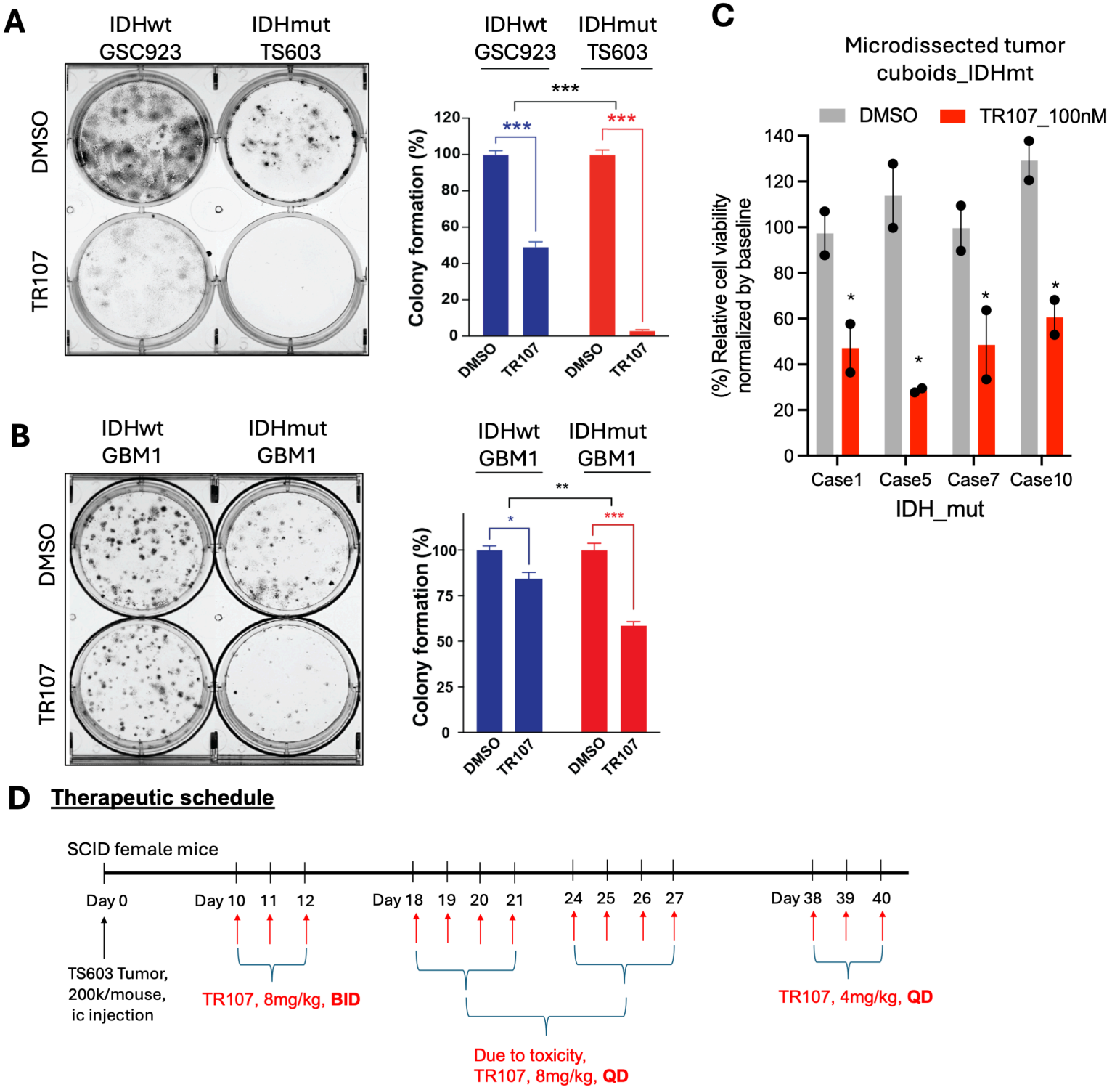
A
IDHwt GSC923
IDHmut TS603
DMSO
TR107
Colony formation (%)
***
B
IDHwt GBM1
IDHmut GBM1
**
*
C
Microdissected tumor cuboids_IDHmt
DMSO
TR107_100nM
(%) Relative cell viability normalized by baseline
Case1
Case5
Case7
Case10
IDH_mut
D
Therapeutic schedule
SCID female mice
Day 0
Day 10 11 12
Day 18 19 20 21
24 25 26 27
Day 38 39 40
TS603 Tumor, 200k/mouse, ic injection
TR107, 8mg/kg, BID
Due to toxicity, TR107, 8mg/kg, QD
TR107, 4mg/kg, QD
E
Probability of Survival
Median survival
Control 45.00
TR107 50.00
Control
TR107
p<0.02
Days Elapsed
F
Vehicle
TR107
Mice tumors
V1 V2 T1 T2 T3
c-Caspase3
TFAM
ATF4
CHOP
TOM20
ACTIN
KDa